Downloaded from http://rsta.royalsocietypublishing.org/ on January 21, 2017

PHILOSOPHICAL TRANSACTIONS OF THE ROYAL SOCIETY A

Phil. Trans. R. Soc. A (2011) **369**, 1670–1686
doi:10.1098/rsta.2010.0228

Review

Quantum criticality and incipient phase separation in the thermodynamic properties of the Hubbard model

By D. Galanakis[1,*], E. Khatami[2], K. Mikelsons[2], A. Macridin[3], J. Moreno[1], D. A. Browne[1] and M. Jarrell[1]

[1]*Department of Physics and Astronomy, Louisiana State University, Baton Rouge, LO 70803, USA*
[2]*Department of Physics, Georgetown University, Washington, DC 20057, USA*
[3]*Fermilab, PO Box 500, Batavia, IL 60510, USA*

Transport measurements on the cuprates suggest the presence of a quantum critical point (QCP) hiding underneath the superconducting dome near optimal hole doping. We provide numerical evidence in support of this scenario via a dynamical cluster quantum Monte Carlo study of the extended two-dimensional Hubbard model. Single-particle quantities, such as the spectral function, the quasi-particle weight and the entropy, display a crossover between two distinct ground states: a Fermi liquid at low filling and a non-Fermi liquid with a pseudo-gap at high filling. Both states are found to cross over to a marginal Fermi-liquid state at higher temperatures. For finite next-nearest-neighbour hopping t', we find a classical critical point at temperature T_c. This classical critical point is found to be associated with a phase-separation transition between a compressible Mott gas and an incompressible Mott liquid corresponding to the Fermi liquid and the pseudo-gap state, respectively. Since the critical temperature T_c extrapolates to zero as t' vanishes, we conclude that a QCP connects the Fermi liquid to the pseudo-gap region, and that the marginal Fermi-liquid behaviour in its vicinity is the analogue of the supercritical region in the liquid–gas transition.

Keywords: quantum criticality; dynamical cluster approximation; cluster methods

1. Introduction

(*a*) *Relevance of quantum criticality in the cuprates*

The unusually high superconducting transition temperature of the hole-doped cuprates [1] remains an unsolved puzzle, despite more than two decades of intense theoretical and experimental research. Pairing, which has a d-wave symmetry and

*Author for correspondence (dimitris.galanakis@gmail.com).

One contribution of 7 to a Theme Issue 'Normal state of the copper oxide high-temperature superconductors'.

 This journal is © 2011 The Royal Society

Downloaded from http://rsta.royalsocietypublishing.org/ on January 21, 2017

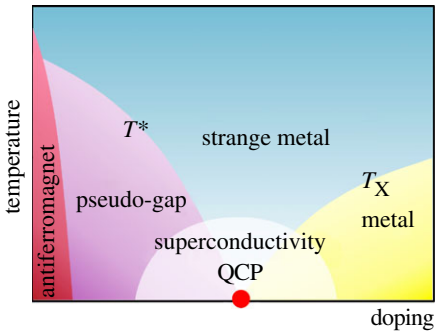

Figure 1. The phase diagram of the cuprates. As a function of temperature and doping, the cuprates display antiferromagnetic order at low doping, a non-Fermi-liquid pseudo-gap region at intermediate doping and a metallic region at higher doping. Around optimal doping, superconductivity develops, and above the superconducting dome, a strange metal with non-Fermi-liquid properties appears. T^* separates the pseudo-gap from the marginal Fermi-liquid phase. T_X is the crossover temperature between the Fermi and the marginal Fermi-liquid regions. A QCP hides underneath the superconducting dome near optimal hole doping. (Online version in colour.)

a short coherence length, but a too high T_c to be accounted for by Bardeen–Cooper–Schrieffer (BCS) theory [2], is not the only unconventional property of these materials. Their phase diagram, shown in figure 1, is a landscape of exotic states of matter. Undoped cuprates are Mott insulators with antiferromagnetic long-range order [3]. Antiferromagnetism collapses upon small doping, and it is replaced by a pseudo-gap state characterized by a suppression of spectral weight along the antinodal direction. Further doping turns the system into a conventional Fermi-liquid metal. Between the Fermi-liquid and the pseudo-gap regions lies a strange metal phase with T-linear resistivity. The superconducting dome emerges in the crossover between the pseudo-gap and the Fermi-liquid regions at lower temperatures.

Strong electronic correlations are the cause of the rich phase diagram of cuprate superconductors [4]. The same strong correlations render traditional theoretical approaches, such as perturbation theory and Fermi-liquid theory, inapplicable. Some recent conceptual progress has been achieved by associating the optimal T_c with a quantum critical point (QCP), lying underneath the superconducting dome and connecting the pseudo-gap and Fermi-liquid regions [5,6]. Unlike a classical critical point, a QCP affects the behaviour of the system in a wide range of temperatures and might explain the emergence of a T-linear resistivity up to room temperature.

Experimental evidence for a QCP comes from transport [7–9] and thermodynamic measurements [10]. Angle-resolved photoemission spectroscopy (ARPES) [11,12] and quantum oscillation measurements [13] show that, in the pseudo-gap region, the Fermi surface consists of small pockets that have a different topology than the large Fermi surface present in the Fermi liquid. It is reasonable to assume that those two states are orthogonal to one another and are connected through a transition or a crossover region. Additional evidence in support of quantum criticality comes from measurements of the Kerr signal in $YBa_2Cu_3O_{6+x}$ by Xia *et al.* [14]. They find that, at the pseudo-gap crossover

Downloaded from http://rsta.royalsocietypublishing.org/ on January 21, 2017

temperature, T^*, a non-zero Kerr signal develops sharply and persists even inside the superconducting dome. This is consistent with earlier neutron-scattering measurements by Fauqué *et al.* [15], which show the development of magnetic order in the pseudo-gap phase.

In this article, we review numerical evidence of quantum criticality in the Hubbard model, the de facto model for the cuprates that appeared in earlier publications. In those cited works, the Hubbard model is solved using the dynamical cluster approximation (DCA) in conjunction with several quantum Monte Carlo (QMC) cluster solvers. In all calculations relevant for the phase diagram, we neglect the superconducting transition. The interplay between the QCP and superconductivity will be discussed in a future publication (S.-X. Yang *et al.* 2010, unpublished data). In this review, we focus on the thermodynamic quantities, such as the entropy and the chemical potential, and also on single-particle quantities, such as the spectral weight and the quasi-particle weight. The thermodynamic properties give unbiased evidence of quantum criticality, whereas single-particle properties may be used to gain more detailed insight on the ground state. Both sets of quantities rely on the evaluation of the self-energy, which can be calculated using quantum cluster methods.

At a critical interaction-dependent filling, we find that the entropy exhibits a maximum, the quasi-particle weight displays a crossover from Fermi-liquid to pseudo-gap behaviour and the spectral function shows a wide saddle-point region crossing the chemical potential. This is consistent with the presence of a QCP, since the lack of an energy scale results in an enhanced entropy at low temperatures. We also find that, by tuning an appropriate control parameter, the next-nearest-neighbour hopping, $t' > 0$, the QCP becomes a classical critical point associated with a phase-separation transition. This QCP affects a very large supercritical region of finite t'. For negative values of t', we believe that the pseudo-gap and the Fermi-liquid regions will be separated by an extended crossover region of doping. We present our findings in two sections. In §2, we discuss the single-particle spectra and the thermodynamic properties of the $t' = 0$ Hubbard model. In §3, we discuss the phase separation in the $t' > 0$ Hubbard model.

(*b*) *Hubbard model*

Shortly after the discovery of high-T_c superconductors, Anderson [16] suggested that the Hubbard model captures the basic properties of the high-temperature superconductors and Zhang & Rice [17] demonstrated that only a single band is needed. The single-band Hubbard model is represented by the Hamiltonian

$$H = -t \sum_{\langle i,j \rangle, \sigma} [c^{\dagger}_{i\sigma} c_{j\sigma} + \text{H.C.}] + U \sum_i n_{i\downarrow} n_{i\uparrow}, \tag{1.1}$$

where $c^{\dagger}_{i\sigma}$ ($c_{i\sigma}$) is the creation (annihilation) operator of an electron at site i and spin σ, $n_{i\sigma}$ is the corresponding number operator, t is the hopping parameter between nearest-neighbour sites and U is the on-site Coulomb repulsion. Despite its apparent simplicity, the Hubbard model is notoriously difficult to solve. No analytical solutions exist except in one dimension [18–20]. However, tremendous theoretical and computational efforts have resulted in approximation schemes that provide access to the physics of this model in higher dimensions. In

Downloaded from http://rsta.royalsocietypublishing.org/ on January 21, 2017

this article, we also discuss results for the generalized Hubbard model that includes hopping between next-nearest neighbours with amplitude t':

$$H = -t \sum_{\langle i,j\rangle,\sigma} [c_{i\sigma}^{\dagger} c_{j\sigma} + \text{H.C.}] - t' \sum_{\langle\langle i,l\rangle\rangle} [c_{i\sigma}^{\dagger} c_{l\sigma} + \text{H.C.}] + U \sum_{i} n_{i\downarrow} n_{i\uparrow}. \tag{1.2}$$

Important progress in our understanding of strongly correlated models has been achieved by the development of finite-size methods, including exact diagonalization and QMC. The latter works well in the simulation of bosonic systems where creation and annihilation operators commute. However, owing to the minus-sign problem associated with the anticommutation relations of fermionic operators, QMC is limited to small lattice sizes and consequently gives questionable predictions for correlated electronic systems in the thermodynamic limit.

Another successful approach is the dynamical mean-field approximation (DMFA), which treats the local dynamical correlations explicitly and non-local (inter-site) correlations in a mean-field approximation [21–24]. This technique becomes exact in the limit of infinite dimensions [25,26]. However, when applied to finite dimensions, the DMFA fails to describe the renormalization effects due to momentum-dependent modes and the transitions to phases with non-local order parameters. Thus, DMFA misses physical phenomena that are abundant in strongly correlated systems, such as the development of spin or charge-density wave phases, localization in the presence of disorder, spin-liquid physics, unconventional superconductivity, etc.

The limitations of the DMFA are addressed by cluster mean-field theories. Those fall into two categories [27]: the cluster dynamical mean-field theory (CDMFT) [28], which is formulated in real space, and the dynamical cluster approximation (DCA) [29], which is formulated in momentum space. In both cases, the system is viewed as a cluster embedded in an effective medium. The formal difference between DCA and CDMFT is that, in real space, the DCA cluster satisfies periodic boundary conditions, whereas the CDMFT cluster is open. The two methods should give the same results for large enough clusters. In this work, we present DCA [29,30] results.

DCA treats short-ranged correlations explicitly, while longer-ranged ones are approximated by the mean field. By increasing the cluster size, the length scale of the explicitly treated correlations can be gradually increased while the calculation remains in the thermodynamic limit. In momentum space, the DCA can easily be conceptualized as the approximation in which the self-energy is calculated using the coarse-grained Green function. QMC-based solvers such as Hirsch–Fye (HFQMC) [31], continuous-time (CTQMC) [32] and determinantal quantum Monte Carlo (DQMC) [33] are used to solve the cluster problem. QMC methods are often formulated in imaginary time and an analytic continuation to real time is necessary to evaluate physical quantities. Fortunately, powerful techniques such as the maximum entropy method (MEM) [34,35] are able to successfully select the most likely solution.

Even though quantum cluster schemes have provided a tremendous breakthrough in our understanding of the Hubbard model, they are also subject to limitations. QMC solvers suffer from the sign problem, which scales exponentially with inverse temperature, interaction strength and cluster size. This limits the

Downloaded from http://rsta.royalsocietypublishing.org/ on January 21, 2017

application of the method to relatively small cluster sizes, higher temperatures and intermediate interactions. The limitation in the cluster size is particularly problematic close to a phase transition where the correlation length diverges. The coarse graining also limits the momentum resolution, which for typical cluster sizes is too small to capture detailed features of the spectra, such as van Hove singularities. For a Fermi liquid, this is not a limitation since the physics is dominated by the low frequencies in which the self-energy is momentum independent. However, intrinsically anisotropic states, such as the pseudo-gap, or possibly the quantum critical (QC) region, can be captured only approximately. Finally, MEM uses Bayesian statistics to find the most likely spectra for the QMC data, subject to sum rules, such as conservation of the spectral weight. Because of the statistical errors in the QMC data, the frequency spectrum resolved using MEM has a limited resolution.

Despite those limitations, progress can be achieved in accessing the QC region by algorithmic optimizations. A truly universal way to deal with the severity of the sign problem is to vastly increase the statistics, using massively parallel QMC algorithms with highly optimized codes.

2. From Fermi liquid to pseudo-gap

A great advantage of the DCA is its ability to evaluate the self-energy as a function of momentum $\mathbf{k}$ and Matsubara frequency $\mathrm{i}\omega_n$, $\Sigma(\mathbf{k}, \mathrm{i}\omega_n)$. From the self-energy, various single-particle quantities, such as the spectral function, $A(\mathbf{k}, \omega)$, the quasi-particle weight, $Z_{\mathbf{k}}$, and the energy can be derived. All those quantities provide insight on the ground state of the system. In this section, we will show how the transition from the Fermi-liquid to the pseudo-gap state is reflected in such single-particle quantities.

(a) *Self-energy*

Typical Matsubara frequency self-energy curves for various values of doping are shown in figure 2. The real part of the self-energy, $\Re\Sigma(\mathrm{i}\omega_n)$, has large momentum dependence in the pseudo-gap region (top right panel), where the opening of the gap along the antinodal direction can be observed. The vanishing of the $\Im\Sigma(\mathrm{i}\omega_n)$ for $\mathrm{i}\omega_n \to 0$ for $n = 0.75$ and $n = 0.85$ is consistent with Fermi-liquid and marginal Fermi-liquid behaviour, respectively. But, in general, it is difficult to see signatures of the physics of the model in the Matsubara frequency self-energy.

(b) *Spectral function*

The single-particle spectral function shows a clear evolution from a Fermi-liquid to a pseudo-gap state as the filling increases towards half-filling. Figure 3 displays a density plot of the spectral function, $A(\mathbf{k}, \omega) = -(1/\pi)\Im G(\mathbf{k}, \omega)$, which is extracted by analytically continuing the imaginary-time Green function. At low filling, $n < 0.85$, the spectral function exhibits a typical Fermi-liquid form. A notable characteristic is the presence of a wide saddle-point region, reminiscent of a van Hove singularity [36], along the antinodal direction. Around the critical filling of $n = 0.85$, this saddle-point feature crosses the chemical potential. This crossing results in a sharp peak in the density of states (DOS) [37], which displays

Downloaded from http://rsta.royalsocietypublishing.org/ on January 21, 2017

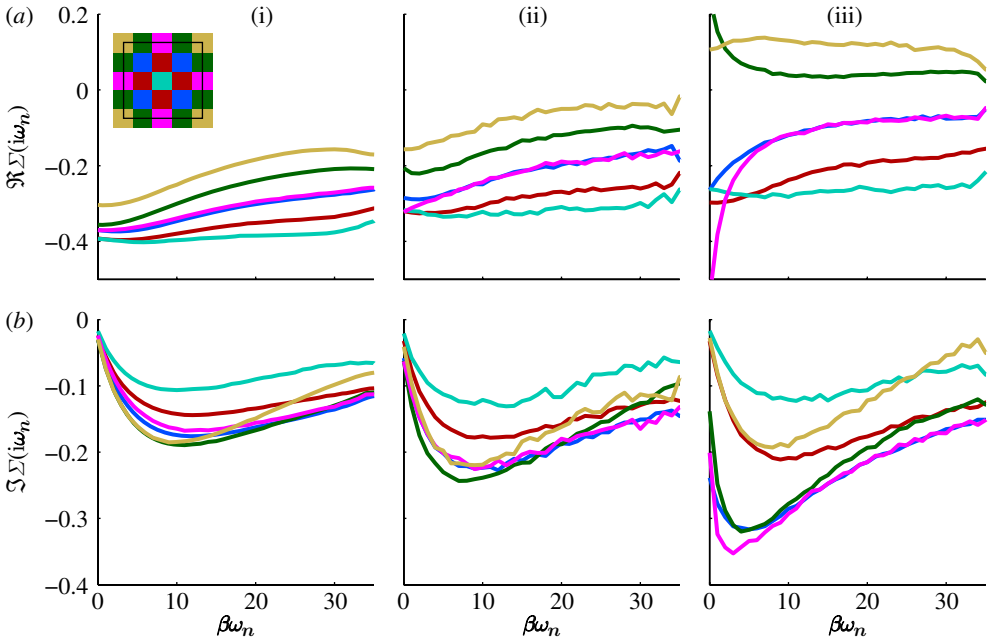

Figure 2. (*a*) Real and (*b*) imaginary components of the cluster self-energy in imaginary time as a function of $\beta\omega_n$ as evaluated by CTQMC for $N_c = 16$, $U = 6t$, $\beta t = 17.5$ and fillings n of (i) 0.75, (ii) 0.85 and (iii) 0.95. The inset in the upper left panel shows a map of the Brillouin zone (enclosed in the square) using different colours for the inequivalent cluster sites. The different self-energy curves correspond to the different sites on the irreducible wedge of the cluster. (Online version in colour.)

low-energy particle–hole symmetry [38]. At higher filling, $n > 0.85$, the spectral weight collapses along the antinodal direction and a pseudo-gap opens. The Fermi surface obtained by extremizing $|\nabla n_{\mathbf{k}}|$ shows a similar evolution (see figure 3*b*). The Fermi-liquid region consists of a large hole pocket, which extends and touches the edges of the Brillouin zone $(0, \pm\pi)$, $(\pm\pi, 0)$ at $n = 0.85$. In the pseudo-gap region, the Fermi surface consists of four Fermi arcs centred around the nodal points, similar to the ones obtained from ARPES. These results clearly demonstrate that the DCA can capture qualitatively the evolution of the ground state from a Fermi-liquid to a pseudo-gap phase.

(*c*) *Quasi-particle weight*

Whereas the spectral function gives a qualitative understanding of the ground state, it relies on the analytic continuation of numerical data. Since extracting quantitative information from analytically continued data is difficult, a more robust approach is to rely on imaginary time quantities, such as the quasi-particle weight $Z(\mathbf{k})$. Since the quasi-particle weight is finite across a Fermi surface, but vanishes if the spectrum is incoherent, it will allow us to clearly distinguish between a Fermi-liquid and a pseudo-gap state. The quasi-particle weight can be directly obtained from the Matsubara frequency self-energy as $Z_0(\mathbf{k}) = [1 - \Im\Sigma(\mathbf{k}, i\omega_0)/\omega_0]^{-1}$, where $\omega_0 = \pi T$ is the lowest fermionic Matsubara frequency.

Downloaded from http://rsta.royalsocietypublishing.org/ on January 21, 2017

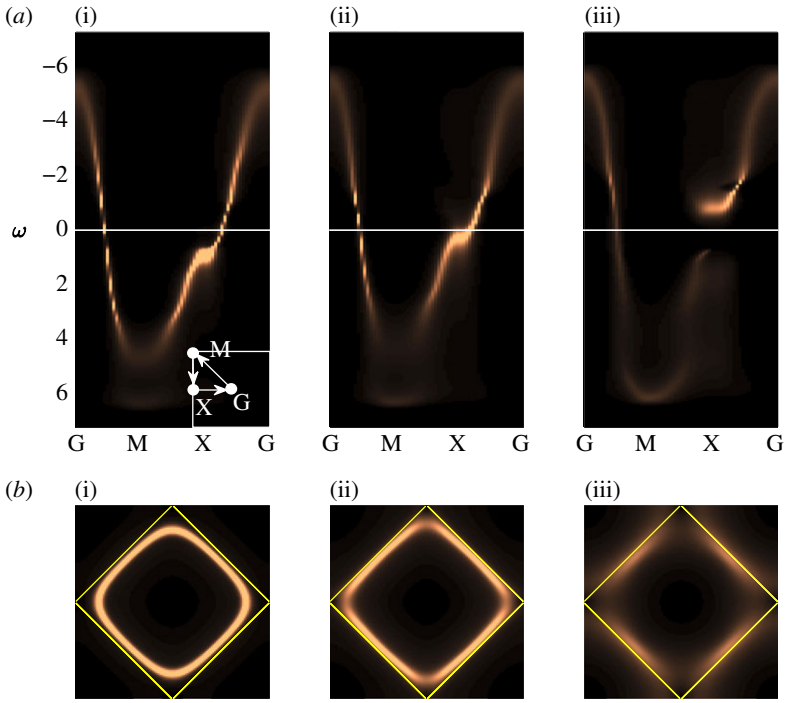

Figure 3. (a) Density plots of the spectral function $A(\mathbf{k},\omega)$ for (i) Fermi-liquid, (ii) marginal Fermi-liquid and (iii) pseudo-gap regions for filling n of (i) 0.75, (ii) 0.85 and (iii) 0.95, respectively, which were obtained by applying MEM on the self-energy of figure 2. The momentum is along the path $\mathrm{G}(0,0) \to \mathrm{M}(\pi,\pi) \to \mathrm{X}(\pi,0) \to \mathrm{G}(0,0)$. Note that the discontinuity along $\mathrm{G}(0,0) \to \mathrm{M}(\pi,\pi)$ in the left and middle panels is an artefact of our interpolation algorithm. A wide saddle-point region between X and G sits above the chemical potential in the Fermi-liquid region and crosses it around the critical filling ($n = 0.85$). In the pseudo-gap region, this feature sits below the chemical potential, leaving a gap along the antinodal direction behind it. (b) Fermi surface as extracted from $|\nabla n_{\mathbf{k}}|$ in (i) Fermi-liquid, (ii) marginal Fermi-liquid and (iii) pseudo-gap regions showing the development of the pseudo-gap in the antinodal direction. The lines mark the magnetic zone boundary. The Coulomb repulsion is $U = 6t$, the temperature $T = 0.069t$ and the cluster size $N_{\mathrm{c}} = 16$. The energy unit is $4t$. (Online version in colour.)

At the limit $T \to 0$ and for a well-behaved self-energy, $Z_0(\mathbf{k})$ converges to the quasi-particle weight, $Z(\mathbf{k})$. Figure 4a displays $Z_{\mathrm{AN}} = Z_0(\omega_0 = \pi T, k \parallel (0,0) \to (0,\pi))$, the Matsubara quasi-particle weight along the antinodal momentum direction for $U = 6t$ and a cluster of size $N_{\mathrm{c}} = 16$ [37]. The momentum $\mathbf{k}$ at the Fermi surface is determined by maximizing $|\nabla n(\mathbf{k})|$. It can be seen that Z_{AN} exhibits two distinguishable behaviours: for $n > n_{\mathrm{c}} = 0.85$ the quasi-particle weight vanishes, whereas it approaches a finite value for $n < n_{\mathrm{c}}$. The $n > n_{\mathrm{c}}$ region corresponds to the pseudo-gap state in which the spectral weight collapses along the antinodal direction, while the $n < n_{\mathrm{c}}$ region behaves as a Fermi liquid.

The temperature dependence of Z_{AN} (figure 4a) not only provides information about the ground state but also allows the extraction of relevant energy scales. By comparing the numerical results with analytical expressions derived from particular phenomenological forms of the self-energy, we obtain T_{X} and T^*. At low filling, $n < n_{\mathrm{c}}$, the high-T dependence of Z_{AN} is best fitted by a marginal

Downloaded from http://rsta.royalsocietypublishing.org/ on January 21, 2017

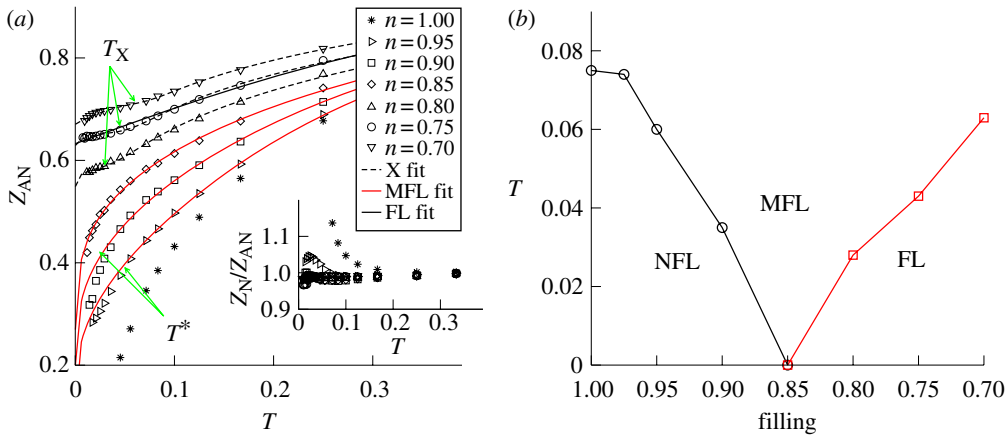

Figure 4. (*a*) The antinodal quasi-particle fraction Z_{AN} as a function of temperature for different values of filling, $U = 6t$ and cluster size $N_c = 16$ (the unit of energy is $4t$). The onset of the pseudo-gap region is determined by the vanishing of the antinodal spectral weight at zero temperature. The dashed and solid lines represent fits of the low-temperature ($T < 0.3$) data to marginal Fermi-liquid (red solid curves), Fermi-liquid (black solid curves) and crossover forms (dashed black curves), respectively. The arrows show the corresponding crossover temperatures T_X and T^*. The value of T^* presented here is obtained from the spin susceptibility as explained in Vidhyadhiraja *et al.* [37], but is consistent with the one extracted from the fitting forms. The ratio Z_N/Z_{AN} of the quasi-particle weight in the nodal (π, π) and antinodal $(0, \pi)$ directions (inset) diverges as the pseudo-gap develops in accordance with figure 3. (*b*) The crossover temperatures T_X (open squares) and T^* (open circles) as a function of filling as extracted from the temperature dependence of Z_{AN} [37] for the same parameters. (Online version in colour.)

Fermi-liquid form, whereas for low T, the data are best fitted by a Fermi liquid. The crossover occurs at a temperature T_X, which is extracted by fitting with a crossover function, and is accompanied by a change in the sign of the curvature of Z_{AN}. At higher filling ($n > 0.85$), the high-temperature Z_{AN} can also be fitted by a marginal Fermi liquid, whereas at low temperatures it cannot. The crossover temperature T^* can be extracted as the lowest temperature at which the marginal Fermi-liquid fit lies within the statistical error. However, a more accurate value can be obtained from the bulk spin susceptibility, which exhibits a peak at T^*, and the two values are found to be consistent [37]. The crossover temperatures T_X and T^* are shown in figure 4*b*. Both of them converge to zero as the filling approaches $n_c = 0.85$, which is the same value for which the peak in the DOS [37] crosses the chemical potential.

(*d*) *Thermodynamics*

A different perspective at the transition from a Fermi-liquid to the pseudo-gap state comes from the evaluation of the entropy [39]. We obtain the entropy by integrating the energy using the formula

$$S(\beta, n) = S(0, n) + \beta E(\beta, n) - \int_0^\beta E(\beta', n)\, \mathrm{d}\beta', \tag{2.1}$$

Downloaded from http://rsta.royalsocietypublishing.org/ on January 21, 2017

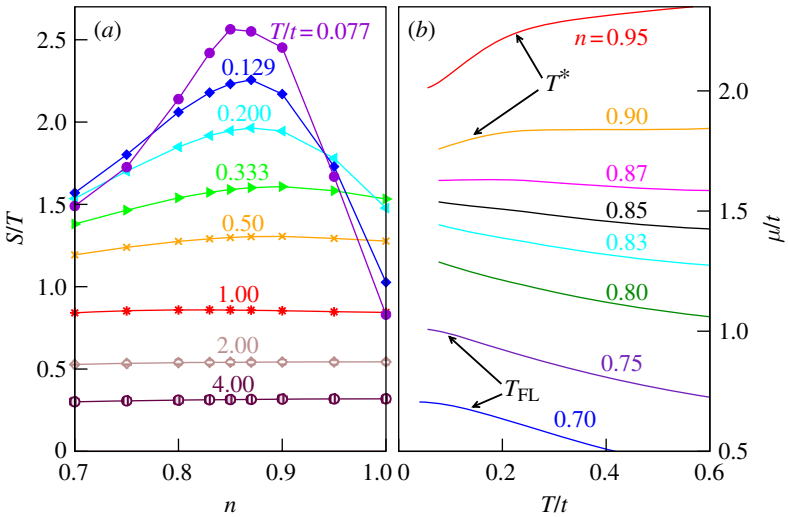

Figure 5. (*a*) The filling dependence of the entropy divided by temperature, S/T, for various temperatures at $U = 6t$ and $N_c = 16$. With decreasing temperature, a peak develops around the critical filling of $n_c = 0.85$. (*b*) The temperature dependence of the chemical potential μ for different fillings. At the critical filling n_c, μ becomes temperature independent at low temperatures. (Online version in colour.)

where β is inverse temperature and $S(0, n)$ is the infinite-temperature entropy. Equation (2.1) is appropriate for QMC calculations, because the integration reduces the statistical error. The challenge is to have good enough statistics to control the error of the surface term, $\beta E(\beta, n)$. In Mikelsons *et al.* [40], large statistics was possible simply by using large computational resources. The entropy divided by the temperature, shown in figure 5*a*, exhibits a maximum at exactly the same critical filling that was identified before from the spectral function and the quasi-particle weight. In figure 5*b*, we show the chemical potential, μ, as a function of temperature. We note that, at the critical filling $\mathrm{d}\mu/\mathrm{d}T = 0$, since the entropy and the chemical potential are related by the Maxwell relation:

$$\left(\frac{\partial S}{\partial n}\right)_{T,U} = -\left(\frac{\partial \mu}{\partial T}\right)_{U,n}. \tag{2.2}$$

Also the temperature dependence of the chemical potential can be used as a practical criterion to identify the location of the critical filling, because evaluating the chemical potential is much less computationally intensive than evaluating the entropy. Using this criterion, we investigate the important question of the dependence of n_c on the Coulomb repulsion U. As shown in figure 6, we find that increasing U reduces the critical filling and thus enlarges the pseudo-gap region in the phase diagram. Our results follow the trend proposed in earlier arguments [38] according to which the critical filling decreases in order to reach the atomic limit value of $n_c = 2/3$.

In this section, we have shown that several single-particle quantities are consistent with the presence of a QCP. The qualitative form of the single-particle spectrum shown in figure 3 is fundamentally different in the Fermi-liquid and the

Downloaded from http://rsta.royalsocietypublishing.org/ on January 21, 2017

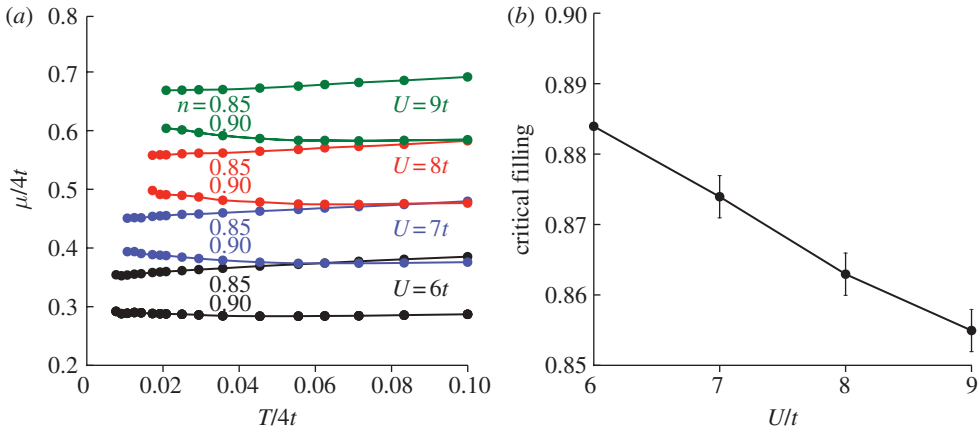

Figure 6. (*a*) The chemical potential as a function of temperature for fillings of $n = 0.85$ and 0.90 and for a variety of interaction strengths U for $N_c = 12$. (*b*) The critical filling, defined by the filling in which $\partial\mu/\partial T = 0$ versus U. The critical filling decreases with U monotonically and is projected to reach the atomic limit value of $n_c = 2/3$ at $U_c = 30t$. (Online version in colour.)

pseudo-gap regions, which points to orthogonal ground states. The temperature dependence of the quasi-particle weight reveals the presence of two crossover temperatures T^* and T_X, which converge to zero at n_c as shown in figure 4*b*. If the crossover temperatures T_X and T^* constitute energy scales that suppress degrees of freedom, their vanishing at n_c means that there are no relevant energy scales to quench the entropy and therefore it collapses at a slower rate, which is consistent with the peak of the entropy observed at n_c. The natural next step to investigate quantum criticality is to access the QCP. However, the fermion-sign problem severely limits the applicability of QMC techniques close to a QCP. It is possible, however, as we will discuss in §3, that by tuning an appropriate control parameter, the critical point may be lifted to finite temperature and thus studied with QMC.

3. Phase separation and quantum criticality

Experiments suggest that cuprate superconductors are susceptible to charge inhomogeneities, such as stripes or chequerboard modulations [41]. These inhomogeneous charge patterns have stimulated intense theoretical and experimental research. Here we will consider the possibility that those charge instabilities are evidence that the cuprates are close to a phase-separation transition, and this proximity may be related to the nature of the QCP.

Our findings suggest that the Hubbard model displays a phase diagram similar to the one for the gas–liquid transition with Mott liquid (ML) and Mott gas (MG) regions. Figure 7*a* shows a possible phase diagram for the Hubbard model as a function of T, $|\mu|$ and n. The red-coloured surface is a schematic of the region where the ML and MG states, characterized by different densities, coexist for $T < T_c$. The critical point is located at temperature T_c, filling n_c and chemical potential μ_c. One can go from one state to the other either smoothly, by avoiding

Downloaded from http://rsta.royalsocietypublishing.org/ on January 21, 2017

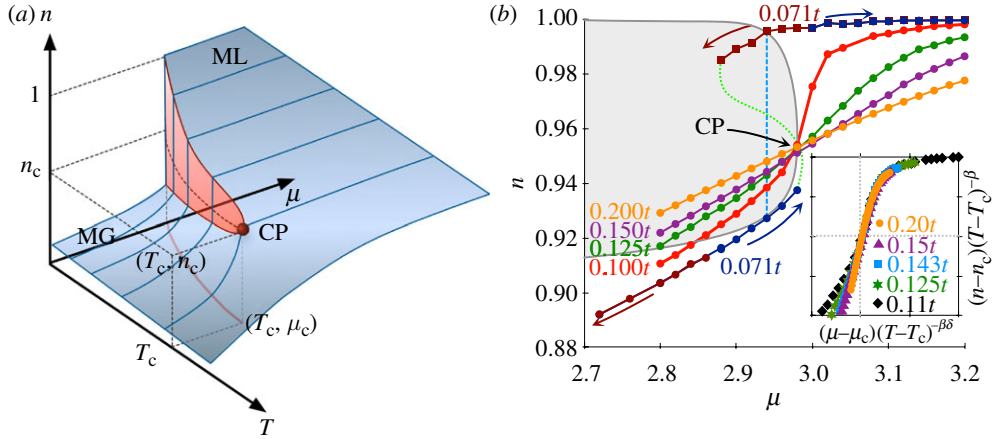

Figure 7. (*a*) The schematic phase diagram in the presence of charge separation. This phase diagram describes the transition between two states labelled Mott liquid (ML) and Mott gas (MG) as a function of temperature T, chemical potential μ, and filling n. The red surface represents the coexistence region, which terminates in a critical point (CP). As we go around the critical point, the state changes smoothly from ML to MG. Along the first-order transition line and for a fixed T and μ, the filling has two values. (*b*) Filling as a function of chemical potential for several temperatures in the vicinity of the charge-separation critical point. The number next to each curve represents the temperature. The coexisting phases are an incompressible Mott liquid at $n \approx 1$ and a compressible Mott gas at $n \approx 0.93$. The critical temperature is $T_c = 0.1t$. The blue dashed line represents the surface of metastability that is not accessible within the DCA. The green dotted line represents the isothermal of the metastable state inside the phase coexistence region (grey zone). At the critical point, the isothermals for $T > T_c$ cross. The inset shows the scaling curve $(n - n_c)(T - T_c)^{-\beta}$ versus $(\mu - \mu_c)(T - T_c)^{-\beta\delta}$ in arbitrary units for $\mu_c = 3t$, $n_c = 0.96$, $T_c = 0.1t$. The scaling exponents, $\beta = 0.10 \pm 0.05$ and $\beta\delta \sim 1$, are roughly consistent with the Ising universality class. (Online version in colour.)

the phase-separation region, or through a first-order transition by crossing it. Right on the phase-separation region, the density has two values for given values of μ and T.

Macridin *et al.* [42] provided compelling evidence of phase separation in the case of the generalized Hubbard model (equation (1.2)) with positive next-nearest-neighbour hopping $t' = 0.3\,t$ and $U = 8t$. Using the DCA in an $N_c = 8$ cluster with HFQMC as the cluster solver, they showed that below a critical temperature $T_c \sim 0.1t$ a first-order transition occurs, which is identified by a hysteresis in the n versus μ curve for $T < T_c$. Hysteresis curves have been used to identify first-order transitions within dynamical mean-field theory [21]. As shown in figure 7*b* with more precise data obtained using DQMC as the cluster solver, the hysteresis is between two states of different filling, the ML at half-filling and the MG at a filling of about 0.93 for $T = 0.071t$. The ML is incompressible and insulating. Its compressibility, which is the slope of the filling versus μ curve in the high-filling side of the hysteresis curve, is small and decreases with temperature. Also, the DOS of the ML phase, shown in figure 8*a*, exhibits a gap as expected for an insulator. On the other hand, the MG is compressible and metallic; the DOS is finite at the chemical potential ($\mu = \omega = 0$), as displayed in figure 8*b*.

Downloaded from http://rsta.royalsocietypublishing.org/ on January 21, 2017

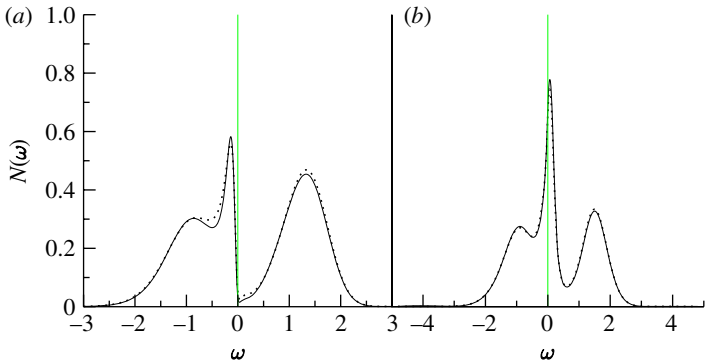

Figure 8. The DOS of (*a*) Mott liquid and (*b*) Mott gas states at $T = 0.077t$ (dotted line) and $T = 0.057$ (solid line). The Mott liquid is an incompressible insulator with a pseudo-gap, while the Mott gas is weakly compressible with a Fermi-liquid peak in the DOS. (Online version in colour.)

The analogy to the well-known phase diagram of a liquid–gas mixture, such as water and steam, is useful to understand this phase transition. At low temperatures, there is a region in the pressure–volume phase diagram in which water and steam coexist for a range of pressures. As the temperature is increased, the region of coexistence contracts and finally terminates at a critical point where the compressibility diverges. In the pressure–temperature phase diagram, this region of coexistence becomes a line of first-order transitions that terminates at a second-order point where the water and gas become indistinguishable and the compressibility diverges. Since the line terminates, it is possible for the system to evolve adiabatically from steam to water without crossing a phase transition line; therefore, the steam and water must have the same symmetry.

In the ML and the MG system, the chemical potential μ replaces the pressure and the density n replaces the volume of the water–gas mixture. Because the order parameter separating the ML from the MG, the density n, does not have a continuous symmetry, order may occur at finite temperatures, and the ML–MG transition will most probably be in the Ising or lattice gas universality class. Within this context, one may then understand the hysteresis of figure 7*b*. The solid lines are isotherms that show how the system evolves with increasing density. At the temperature $T = T_c$, the compressibility diverges at the critical filling. As the temperature is lowered further, there is a region where the ML and MG coexist. Inside this region, the isothermals contain unphysical regions of negative compressibility (dashed line in figure 7*b*) along with metastable regions of positive compressibility. The metastable branch of the isothermal in the vicinity of the ML is a 'supercooled' ML, whereas the one in the vicinity of the MG is a 'superheated' MG. The translational invariance of DCA along with the stabilizing effect of the mean-field host enables access to those metastable states. However, the real physical system will phase separate and the two phases will coexist in equilibrium (dotted line in figure 7*b*).

We can sketch the phase diagram in the T–μ plane using the analogy to the water–steam mixture. The most generally applicable rule governing the shape of phase diagrams was established by Gibbs. For a system of c conserved components and f phases, the Gibbs constraint is given by the relation $\Phi = c - f + 2$, where Φ

Downloaded from http://rsta.royalsocietypublishing.org/ on January 21, 2017

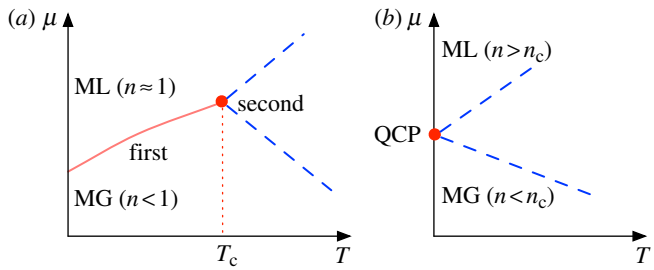

Figure 9. (*a*) The chemical potential–temperature phase diagram of the ML and MG mixture for $t' > 0$. The ML and MG coexist on a line of first-order transitions with positive slope. Since ML and MG have the same symmetry, this line can terminate in a second-order critical point. The blue dashed lines define the boundaries of the supercritical region where the ML and MG cannot be distinguished. Outside this region, either the ML or MG character dominates. (*b*) The chemical potential–temperature phase diagram for $t' \to 0$. The first-order line is absent but supercritical region remains as a QC region. In the Hubbard model, the lines T^* and T_X (figure 4*b*) define the boundaries of this region. For negative values of t', the ML and MG regions will be separated by an extended crossover region of doping. (Online version in colour.)

is the number of independent variables needed to specify the state of every phase. In this case, as in the water–steam system, the number of components $c = 1$, since the particle number is conserved. At a location in the phase diagram where only one phase exists, $\Phi = 1 - 1 + 2 = 2$, so there are two independent variables, and the phase diagram is a surface on the μ, T and n three-dimensional space. There will be places in the phase diagram where two phases exist simultaneously; then $\Phi = 1 - 2 + 2 = 1$, implying that two phases coexist only along lines in the phase diagram. At the lines in the T–μ plane where two phases coexist, n is also determined for each phase, but its value can be different. That is a line of first-order transitions.

Additional information about the lines of first-order transitions is obtained from Clapeyron's equation. The Gibbs free energy $G = E - TS - \mu N$, and $\mathrm{d}G = -S\,\mathrm{d}T - N\,\mathrm{d}\mu$, must be the same for the coexisting phases on a line. If we label the two phases 1 and 2, then

$$(S_1 - S_2)\,\mathrm{d}T = -(N_1 - N_2)\,\mathrm{d}\mu. \tag{3.1}$$

If we identify the latent heat $L = (S_1 - S_2)T$, then $\mathrm{d}\mu/\mathrm{d}T = -L/(T\Delta n)$ represents the slope of the first-order transition line. Since the latent heat L of going from ML to MG is positive, but $\mathrm{d}n$ is negative, the slope $\mathrm{d}\mu/\mathrm{d}T$ of the line of first-order transitions is positive.

Above the critical point terminating the ML–MG transition, the system displays supercritical behaviour in a region where the gas and the liquid cannot be distinguished thermodynamically (cf. figure 9). It is possible for the system to evolve adiabatically through an anticlockwise path from deep in the MG region, through the supercritical region, into the ML region. At the lower edge of the supercritical region, the system loses the Fermi-liquid character of the MG, and at the upper edge, it begins to acquire the pseudo-gap character of the ML.

Downloaded from http://rsta.royalsocietypublishing.org/ on January 21, 2017

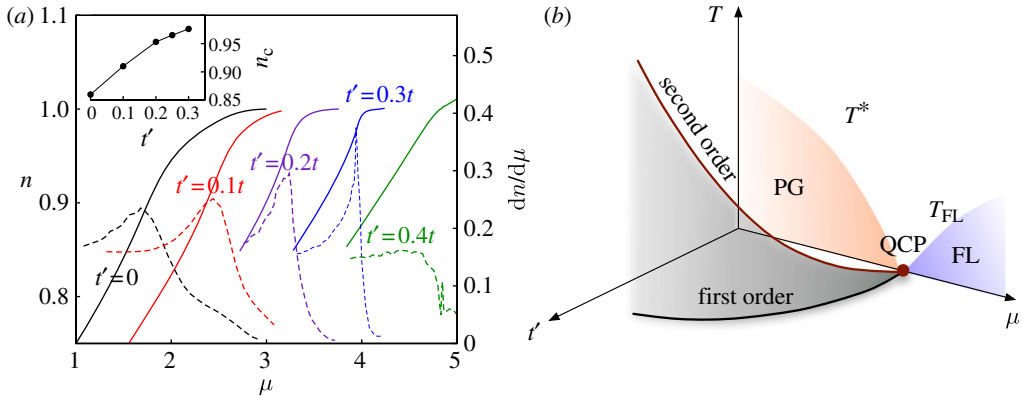

Figure 10. (*a*) Filling, n, versus chemical potential, μ, for $T = 0.077t$, $N_c = 16$, $U = 6t$ and various t' is shown in solid lines and the compressibility, $dn/d\mu$, in dashed lines. A critical filling, identified by the peak in the compressibility, appears at higher temperatures and fillings as t' is increased. The inset shows the t' dependence of the critical filling, n_c. (*b*) Schematic phase diagram of the Hubbard model in the μ, t' and T space (neglecting superconductivity). The classical critical point turns asymptotically into a QCP as $t' \to 0$. (Online version in colour.)

Let us discuss now how this phase separation, which occurs at finite temperature, is related to quantum criticality. The key parameter is the next-nearest-neighbour hopping, t'. For $t' = 0$, there is no evidence for phase separation at finite T, but such a phase separation occurs for positive t'. Khatami *et al.* [43] performed a systematic analysis of the phase diagram of the extended Hubbard model as a function of t'. As shown in figure 10*a*, the compressibility, $\chi_c = dn/d\mu$, exhibits a peak for all positive t' at a critical filling that depends on t'. The width of the peak measures the distance from the critical temperature: the sharper the peak, the closer to T_c the employed temperature is. We see that the critical temperature increases with t' and it starts from $T_c = 0$ at $t' = 0$. These results point to the phase diagram of figure 10*b*. At a positive t', a charge separation occurs at temperatures $T < T_c(t')$ and at a critical filling $n_c(t')$ between an incompressible and insulating ML and a compressible metallic MG. Right at T_c, there is a terminating second-order critical point. By decreasing t', this second-order critical point is pushed down to lower temperatures. Presumably, the line of second-order critical points terminates at the QCP.

Such a scenario constitutes a new path to quantum criticality as it is closely tied to charge fluctuations rather than spin fluctuations. However, numerous simulations suggest that a finite positive t' enhances antiferromagnetic correlations, and since phase separation is only present for $t' > 0$, it suggests that it is driven by strong spin correlations. In addition, previous simulations incorporating Holstein phonons to the Hubbard model found that phonons also enhance the phase-separation instability [44]. As $t'/t \to 0$ (and the electron–phonon coupling vanishes), the phase-separation critical point approaches zero temperature, becoming a QCP. Here, the first-order behaviour is absent from the phase diagram (figure 4*b*), leaving only the adiabatic path from the ML to the MG, which passes through the supercritical region, which is now the QC region. The crossover scale T_X and the pseudo-gap scale T^* are now understood as the boundaries of the QC region. As we cross the line of T^* from the QC region

Downloaded from http://rsta.royalsocietypublishing.org/ on January 21, 2017

into the ML region, the characteristics of the ML become apparent, including the pseudo-gap in the DOS and the insulating behaviour. As we cross the line of T_X from the QC region into the MG, the characteristics of the MG become apparent, including Fermi-liquid formation.

Those calculations certainly do not elucidate the nature of the ML and MG states in real materials. The long-ranged nature of the Coulomb interaction prevents true charge-separated states, but the phase separation we observe may also correspond to other charge instabilities, such as stripes or chequerboard patterns. To distinguish between different charge instabilities, systematic calculations in much larger clusters are necessary, which are not practicable at the moment. However, whatever the type of order, those calculations provide convincing evidence for the existence of a first-order transition at low temperatures. Such a transition is similar to the liquid–gas or the ferromagnetic transition, and its phase diagram would look like figure 7*a*: a first-order line of coexistence that terminates at a critical point at a critical temperature T_c and a critical filling n_c.

4. Conclusions

The presence of a QCP at finite filling in the cuprate phase diagram is a topic of active theoretical and experimental research. Quantum cluster methods are able to shed some light on this phase diagram. By studying single-particle quantities for $t' = 0$, such as the spectral function and the entropy, it can be shown that a Fermi-liquid region at low filling and the pseudo-gap region at higher filling have different spectral signatures, and are connected through an intermediate 'marginal Fermi-liquid' region of maximal entropy. Owing to limitations of QMC, the ground state and quantum criticality are not accessible. We also neglect the superconducting phase transition. The connection with quantum criticality is established by switching on t'. For positive t', a classical critical point emerges at finite temperature T_c, which increases with t'. We note that t' is not the only control parameter that may be able to tune the critical point to finite temperatures, but other parameters, such as phonon coupling, may have the same effect. The phase diagram around the critical point is similar to that of the gas–liquid transition, where the incompressible ML and the compressible MG are the coexisting phases. The strange metal region in this context may be viewed as the supercritical region lying in the vicinity of the critical point. Within the scenario we presented, the pseudo-gap region is not characterized by an order parameter; rather, it must have the same symmetry as the Fermi liquid and the marginal Fermi liquid, since these regions are connected by an adiabatic path in the T–μ phase diagram. Further investigation is necessary to fully characterize the pseudo-gap region, and also to investigate the connection of those results with other scenarios of quantum criticality.

We would like to thank R. Gass, S. Kivelson, D. J. Scalapino, A. M. Tremblay, C. Varma, M. Vojt, S. R. White and J. Zaanen for useful discussions that helped during the development of the presented work. This research was supported by NSF DMR-0706379, DOE CMSN DE-FG02-08ER46540 and by the DOE SciDAC grant DE-FC02-06ER25792. This research used resources of the National Center for Computational Sciences at Oak Ridge National Laboratory, which is supported by the Office of Science of the US Department of Energy under contract no. DE-AC05-00OR22725.

Downloaded from http://rsta.royalsocietypublishing.org/ on January 21, 2017

References

1 Bednorz, J. & Müller, K. 1986 Possible high T_c superconductivity in the Ba–La–Cu–O system. *Z. Phys. B* **64**, 189–193. (doi:10.1007/BF01303701)

2 Bardeen, J., Cooper, L. N. & Schrieffer, J. R. 1957 Microscopic theory of superconductivity. *Phys. Rev.* **106**, 162–164. (doi:10.1103/PhysRev.106.162)

3 Néel, L. 1949 Preuves expérimentales du ferromagnétisme et de l'antiferromagnétisme. *Ann. Inst. Fourier* **1**, 163–183.

4 Phillips, P. 2010 Colloquium: identifying the propagating charge modes in doped Mott insulators. *Rev. Mod. Phys.* **82**, 1719–1742. (doi:10.1103/RevModPhys.82.1719)

5 Broun, D. M. 2008 What lies beneath the dome? *Nat. Phys.* **4**, 170–172. (doi:10.1038/nphys909)

6 Sachdev, S. 2010 Where is the quantum critical point in the cuprate superconductors? *Phys. Status Solidi B* **247**, 537–543. (doi:10.1002/pssb.200983037)

7 Balakirev, F. F., Betts, J. B., Migliori, A., Tsukada, I., Ando, Y. & Boebinger, G. S. 2009 Quantum phase transition in the magnetic-field-induced normal state of optimum-doped high-T_c cuprate superconductors at low temperatures. *Phys. Rev. Lett.* **102**, 017004. (doi:10.1103/PhysRevLett.102.017004)

8 Daou, R. *et al.* 2009 Linear temperature dependence of resistivity and change in the Fermi surface at the pseudogap critical point of a high-T_c superconductor. *Nat. Phys.* **5**, 31–34. (doi:10.1038/nphys1109)

9 van der Marel, D. *et al.* 2003 Quantum critical behaviour in a high-T_c superconductor. *Nature* **425**, 271. (doi:10.1038/nature01978)

10 Bernhard, C., Tallon, J. L., Blasius, T., Golnik, A. & Niedermayer, C. 2001 Anomalous peak in the superconducting condensate density of cuprate high-T_c superconductors at a unique doping state. *Phys. Rev. Lett.* **86**, 1614–1617. (doi:10.1103/PhysRevLett.86.1614)

11 Platé, M. *et al.* 2005 Fermi surface and quasiparticle excitations of overdoped $Tl_2Ba_2CuO_{6+\delta}$. *Phys. Rev. Lett.* **95**, 077001. (doi:10.1103/PhysRevLett.95.077001)

12 Shen, K. M. *et al.* 2005 Nodal quasiparticles and antinodal charge ordering in $Ca_{2-x}Na_xCuO_2Cl_2$. *Science* **307**, 901–904. (doi:10.1126/science.1103627)

13 Doiron-Leyraud, N., Proust, C., Leboeuf, D., Levallois, J., Bonnemaison, J.-B., Liang, R., Bonn, D. A., Hardy, W. N. & Taillefer, L. 2007 Quantum oscillations and the Fermi surface in an underdoped high-T_c superconductor. *Nature* **447**, 565–568. (doi:10.1038/nature05872)

14 Xia, J. *et al.* 2008 Polar Kerr-effect measurements of the high-temperature $YBa_2Cu_3O_{6+x}$ superconductor: evidence for broken symmetry near the pseudogap temperature. *Phys. Rev. Lett.* **100**, 127002. (doi:10.1103/PhysRevLett.100.127002)

15 Fauqué, B., Sidis, Y., Hinkov, V., Pailhès, S., Lin, C. T., Chaud, X. & Bourges, P. 2006 Magnetic order in the pseudogap phase of high-T_c superconductors. *Phys. Rev. Lett.* **96**, 197001. (doi:10.1103/PhysRevLett.96.197001)

16 Anderson, P. W. 1987 The resonating valence bond state in La_2CuO_4 and superconductivity. *Science* **235**, 1196–1198. (doi:10.1126/science.235.4793.1196)

17 Zhang, F. C. & Rice, T. M. 1988 Effective Hamiltonian for the superconducting Cu oxides. *Phys. Rev. B* **37**, 3759. (doi:10.1103/PhysRevB.37.3759)

18 Frahm, H. & Korepin, V. E. 1990 Critical exponents for the one-dimensional Hubbard model. *Phys. Rev. B* **42**, 10 553–10 565. (doi:10.1103/PhysRevB.42.10553)

19 Kawakami, N. & Yang, S.-K. 1990 Correlation functions in the one-dimensional t–J model. *Phys. Rev. Lett.* **65**, 2309–2311. (doi:10.1103/PhysRevLett.65.2309)

20 Lieb, E. H. & Wu, F. Y. 1968 Absence of Mott transition in an exact solution of the short-range, one-band model in one dimension. *Phys. Rev. Lett.* **20**, 1445–1448. (doi:10.1103/PhysRevLett.20.1445)

21 Georges, A., Kotliar, G., Krauth, W. & Rozenberg, M. J. 1996 Dynamical mean-field theory of strongly correlated fermion systems and the limit of infinite dimensions. *Rev. Mod. Phys.* **68**, 13–125. (doi:10.1103/RevModPhys.68.13)

22 Metzner, W. & Vollhardt, D. 1989 Correlated lattice fermions in $d = \infty$ dimensions. *Phys. Rev. Lett.* **62**, 324–327. (doi:10.1103/PhysRevLett.62.324)

Downloaded from http://rsta.royalsocietypublishing.org/ on January 21, 2017

23 Müller-Hartmann, E. 1989 Correlated fermions on a lattice in high dimensions. *Z. Phys. B* **74**, 507–512. (doi:10.1007/BF01311397)
24 Müller-Hartmann, E. 1989 The Hubbard model at high dimensions: some exact results and weak coupling theory. *Z. Phys. B* **76**, 211–217. (doi:10.1007/BF01312686)
25 Georges, A. & Kotliar, G. 1992 Hubbard model in infinite dimensions. *Phys. Rev. B* **45**, 6479–6483. (doi:10.1103/PhysRevB.45.6479)
26 Jarrell, M. 1992 Hubbard model in infinite dimensions: a quantum Monte Carlo study. *Phys. Rev. Lett.* **69**, 168–171. (doi:10.1103/PhysRevLett.69.168)
27 Maier, T., Jarrell, M., Pruschke, T. & Hettler, M. 2005 Quantum cluster theories. *Rev. Mod. Phys.* **77**, 1027. (doi:10.1103/RevModPhys.77.1027)
28 Kotliar, G., Savrasov, S. Y., Pálsson, G. & Biroli, G. 2001 Cellular dynamical mean field approach to strongly correlated systems. *Phys. Rev. Lett.* **87**, 186401. (doi:10.1103/PhysRevLett.87.186401)
29 Hettler, M. H., Tahvildar-Zadeh, A. N., Jarrell, M., Pruschke, T. & Krishnamurthy, H. R. 1998 Nonlocal dynamical correlations of strongly interacting electron systems. *Phys. Rev. B* **58**, R7475–R7479. (doi:10.1103/PhysRevB.58.R7475)
30 Hettler, M. H., Mukherjee, M., Jarrell, M. & Krishnamurthy, H. R. 2000 Dynamical cluster approximation: nonlocal dynamics of correlated electron systems. *Phys. Rev. B* **61**, 12 739–12 756. (doi:10.1103/PhysRevB.61.12739)
31 Hirsch, J. & Fye, R. 1986 Monte Carlo method for magnetic impurities in metals. *Phys. Rev. Lett.* **56**, 2521–2524. (doi:10.1103/PhysRevLett.56.2521)
32 Rubtsov, A., Savkin, V. & Lichtenstein, A. 2005 Continuous-time quantum Monte Carlo method for fermions. *Phys. Rev. B* **72**, 035122. (doi:10.1103/PhysRevB.72.035122)
33 Blankenbecler, R., Scalapino, D. J. & Sugar, R. L. 1981 Monte Carlo calculations of coupled boson–fermion systems. I. *Phys. Rev. D* **24**, 2278–2286. (doi:10.1103/PhysRevD.24.2278)
34 Gubernatis, J. E., Jarrell, M., Silver, R. N. & Sivia, D. S. 1991 Quantum Monte Carlo simulations and maximum entropy: dynamics from imaginary-time data. *Phys. Rev. B* **44**, 6011–6029. (doi:10.1103/PhysRevB.44.6011)
35 Jarrell, M. & Gubernatis, J. E. 1996 Bayesian inference and the analytic continuation of imaginary-time quantum Monte Carlo data. *Phys. Rep.* **269**, 133–195. (doi:10.1016/0370-1573(95)00074-7)
36 Radtke, R. J. & Norman, M. R. 1994 Relation of extended Van Hove singularities to high-temperature superconductivity within strong-coupling theory. *Phys. Rev. B* **50**, 9554–9560. (doi:10.1103/PhysRevB.50.9554)
37 Vidhyadhiraja, N. S., Macridin, A., Şen, C., Jarrell, M. & Ma, M. 2009 Quantum critical point at finite doping in the 2D Hubbard model: a dynamical cluster quantum Monte Carlo study. *Phys. Rev. Lett.* **102**, 206407. (doi:10.1103/PhysRevLett.102.206407)
38 Chakraborty, S., Galanakis, D. & Phillips, P. 2008 Emergence of particle–hole symmetry near optimal doping in high-temperature copper oxide superconductors. *Phys. Rev. B* **82**, 214503. (doi:10.1103/PhysRevB.82.214503)
39 Bonča, J. & Prelovšek, P. 2003 Thermodynamics of the planar Hubbard model. *Phys. Rev. B* **67**, 085103. (doi:10.1103/PhysRevB.67.085103)
40 Mikelsons, K., Khatami, E., Galanakis, D., Macridin, A., Moreno, J. & Jarrell, M. 2009 Thermodynamics of the quantum critical point at finite doping in the two-dimensional Hubbard model studied via the dynamical cluster approximation. *Phys. Rev. B* **80**, 140505. (doi:10.1103/PhysRevB.80.140505)
41 Hinkov, V. *et al.* 2004 Two-dimensional geometry of spin excitations in the high-transition-temperature superconductor $YBa_2Cu_3O_{6+x}$. *Nature* **430**, 650–654. (doi:10.1038/nature02774)
42 Macridin, A., Jarrell, M. & Maier, T. 2006 Phase separation in the Hubbard model using the dynamical cluster approximation. *Phys. Rev. B* **74**, 085104. (doi:10.1103/PhysRevB.74.085104)
43 Khatami, E., Mikelsons, K., Galanakis, D., Macridin, A., Moreno, J., Scalettar, R. T. & Jarrell, M. 2010 Quantum criticality due to incipient phase separation in the two-dimensional Hubbard model. *Phys. Rev. B* **81**, 201101. (doi:10.1103/PhysRevB.81.201101)
44 Macridin, A. & Jarrell, M. 2009 Isotope effect in the Hubbard model with local phonons. *Phys. Rev. B* **79**, 104517. (doi:10.1103/PhysRevB.79.104517)